



Cite this: *React. Chem. Eng.*, 2025, **10**, 1291

## Gas–liquid flow synthesis of $\text{Zn}_3\text{N}_2$ -quantum dots†

Malin G. Lüdicke, \* Jonas Schramm, Martin Wichert and Ralph A. Sperling \*

Received 11th November 2024,  
Accepted 17th February 2025

DOI: 10.1039/d4re00548a

rsc.li/reaction-engineering

Continuous process engineering leads production of fine chemicals to a new level of industrialisation. This study elaborates specifications, benefits and pitfalls for the biphasic, high-temperature synthesis of  $\text{Zn}_3\text{N}_2$  quantum dots, which are made from inexpensive and earth-abundant starting materials. A micro-flow tubular reactor equipped with inline/online process sensors and a product analysis device is used. All technical requirements are fulfilled for the corrosive gas and air-sensitive starting and product materials to create a safe pilot plant for reproducible nanoparticle synthesis. The process parameter window yields tunable fluorescent nanocrystals (506–710 nm, 4–10 nm) which broadly match in quality (FWHM: 99–186 nm, QY: 15–56%) with those made in a batch approach. The transfer to a continuous synthesis practice greatly improves throughput because time is reduced as the reaction scheme can be realised in a single process step. In addition, handling effort is minimised with inline reagent dilution and optical spectroscopy which allows product adaptation by tuning of the process parameters in real-time.

## Introduction

The transfer from batch to flow reaction synthesis is in the making for nanoparticulate systems like quantum dots (QDs), because of the process-related advantages. These are increased safety, scalability and most importantly, tight control over parameters and product quality. Colloidal QDs consist of a semiconductor core, stabilised by organic surfactants. Their exciton properties are strongly correlated with the nanoparticle size. Therefore, size control leads to tunable emission wavelengths, that light-emitting applications rely on in research and industry.<sup>1–5</sup>

Fig. 1 visualises this tunable spectral coverage of core QDs based on three element classes which were manufactured with advanced reactor designs resulting in major progress. For example, K. Watanabe *et al.* detailed the emission tunability of CdSe in very small graduations varying six synthesis factors including reactor parameters like the flow rates.<sup>6</sup> Two research groups exploited the technical opportunities of flow-chemistry when applying solvothermal conditions which allowed the use of low-boiling fluids.<sup>7–9</sup> This approach can bypasses the down-streaming process and separation of the product from commonly high-boiling solvents with respect to the whole production chain. Plus, the results indicate a higher product quality by means of a low particle size distribution. Generally, reaction times could be reduced due to the increased mass and heat transfer in a

tube compared to a batch reactor. This led to high margins as demonstrated by A. Nightingale *et al.* who synthesised 54 g dried CdTe QDs powder. It is worth to note the very low emission oscillation of  $\pm 1$  nm during the 9 h run.<sup>10</sup> Besides that, integration of *in situ* analysis devices allowed assessment and thus adaptation of process conditions in real-time. Furthermore relevant reaction mechanism details were disclosed based on photoluminescence or diffraction data, like stepwise nucleation mechanisms and corresponding reaction time constants.<sup>11–13</sup> Among these selected works, some research groups constructed pilot plants with most modules being computer-controlled.<sup>6,14–17</sup> Automation is an adjoining step of the continuous QDs

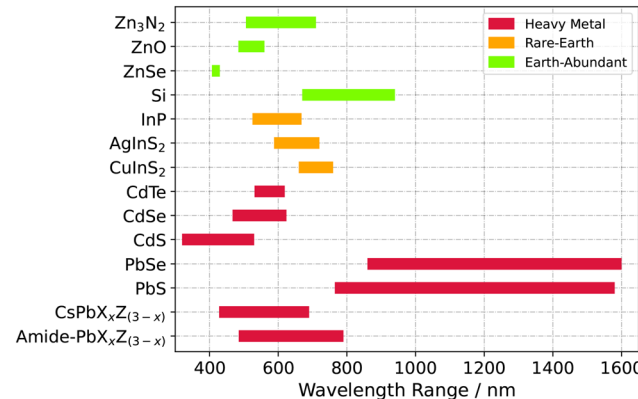


**Fig. 1** Collection of semiconductor QDs systems produced with flow-chemistry and their adjustable fluorescence emission maxima known from literature. To the best of our knowledge, a continuous synthesis process for  $\text{Zn}_3\text{N}_2$  QDs is evaluated for the first time in this study. It is based on non-toxic, earth abundant elements and inexpensive precursors.

Fraunhofer Institute for Microengineering and Microsystems IMM, Carl-Zeiss-Strasse 18-20, 55129 Mainz, Germany. E-mail: malin.luedicke@posteo.de, ralph.sperling@imm.fraunhofer.de

† Electronic supplementary information (ESI) available. See DOI: <https://doi.org/10.1039/d4re00548a>



synthesis development because it increases the level of protection for operators, especially if supercritical or hazardous raw materials are used. Furthermore, it simplifies multivariate screening studies<sup>6,17</sup> and fine-tuning of product features with the help of instrumentation and controlling techniques.<sup>14</sup> The combination with neuronal network algorithms has also been demonstrated to predict condition–property relationships.<sup>15,16</sup>

From a technical point of view, the transfer from batch to continuous synthesis has not yet been evaluated for  $\text{Zn}_3\text{N}_2$  QDs. Therefore, the aim of this study is to demonstrate this transfer and to discuss the challenges and benefits for this material group.

From a material point of view, the raw resources for  $\text{Zn}_3\text{N}_2$  are based on non-heavy metal, earth abundant elements and inexpensive precursors. Among semiconductor materials, this is the minority (Fig. 1). Therefore, once finalised for application, this material class offers a more economic and sustainable alternative to In- or Cd/Pb-based ones which lie in a similar wavelength range ( $\text{ZnO}$ ,<sup>18,19</sup>  $\text{ZnSe}$ ,<sup>20</sup>  $\text{Si}$ ,<sup>21,22</sup>  $\text{InP}$ ,<sup>23,24</sup>  $\text{AgInS}_2$ ,<sup>25,26</sup>  $\text{CuInS}_2$ ,<sup>27,28</sup>  $\text{PbS}$  and  $\text{PbSe}$ ,<sup>29,30</sup>  $\text{CdS}$ ,<sup>31,32</sup>  $\text{CdTe}$ ,<sup>10,33</sup>  $\text{CdSe}$ ,<sup>6</sup>  $\text{CsPbX}_x\text{Z}_{(3-x)}$ ,<sup>16,34</sup> amide– $\text{PbX}_x\text{Z}_{(3-x)}$ <sup>35,36</sup>).

Not many research groups have contributed to the overall comprehension of  $\text{Zn}_3\text{N}_2$  QDs so far. To the best of our knowledge, P. Taylor *et al.* has initially introduced colloidal  $\text{Zn}_3\text{N}_2$  (ref. 37) after various works had been published about polycrystalline thin films or nanowires.<sup>38–41</sup> Most recently, S. Carter-Searjeant and co-workers achieved the nanoparticulate alloy Li–Zn–N/ZnO starting the synthesis with mere solid and liquid precursors<sup>42</sup> while  $\text{Zn}_3\text{N}_2$  nanoparticles evolved intermediary as a side-product, *i.e.* with rather small yield. Besides that, Ahumada-Lazo *et al.* analysed the optical properties of  $\text{Zn}_3\text{N}_2$  in more depth using transient-absorption spectroscopy.<sup>43</sup> In brief, their study indicates a rather weak quantum confinement in correlation to increasing particle size (3.8, 5.8, 8.9 nm) based on three data points with biexciton auger lifetimes (3.2–5.0 ps) and absorption cross sections ( $1.22\text{--}2.04 \times 10^{-15} \text{ cm}^2$ ), respectively. In this context, oleylamine was used as the surfactant which donates two electrons for bonding to passivate partial charges at the crystal phase boundary which in turn reduces non-radiative decay. Chemically, the surfactant is a primary amine, a Lewis base or L-type ligand. Empirically, the alkyl chain (C14) of the molecule provides steric hindrance and thus shielding to maintain colloidal stability. Besides oleylamine, literature provides more ligand candidates that show sufficient steric characteristic while they exhibit a stronger base activity for bonding to increase the quantum yield,<sup>44,45</sup> that could be applied to the  $\text{Zn}_3\text{N}_2$ .

With respect to the electronic structure of  $\text{Zn}_3\text{N}_2$ , its strong oxygen- and water-sensitivity results in the need for carefully performed sample synthesis and investigation. In this context, A. Trapalis *et al.* presented a systematic structure–property study to juxtapose species involved,  $\text{N}_2$ -deficiency and oxidised phases. According to their results,  $\text{Zn}_3\text{N}_2$  can be considered to be a direct semiconductor with a

band gap of 1.31–1.38 eV in bulk when stoichiometric while the bandgap is significantly larger after oxidation.<sup>40,46</sup> Still, the fast oxidation rate of  $\text{Zn}_3\text{N}_2$  results in high precautionary effort during all handling steps: synthesis, spectral analysis and downstream processing.

Here, continuous flow practices can contribute in handling the issue with time-resolved analytical and gas-closed setups. Furthermore, a tube reactor design can be beneficial for the reaction course as the ammonia gas is captured in the reaction medium which in turn increases the contact area between both precursors. Therefore, the central aim of this study is to manufacture  $\text{Zn}_3\text{N}_2$  QDs in a microflow reactor, while controlling the optical properties of the product by tuning process parameters. The new synthesis approach is compared to batch results taking into account the inherent product quality and the reaction and measurement necessities. As starting point, the previously reported batch synthesis is reproduced.<sup>37</sup> Next, the continuous reactor and synthesis process are realised, introducing diethylzinc ( $\text{ZnEt}_2$ ) and  $\text{NH}_3$  in a biphasic flow with either fixed concentrations or variable dosing of  $\text{ZnEt}_2$ . Furthermore, an online analysis module is integrated directly at the reactor outlet. Offline fluorescence emission analysis is compared alongside, to finally unfold the process parameter room to adjust the properties at different temperatures, concentration levels and average residence times.

## Results and discussion

### Batch synthesis

The batchwise synthesis protocol<sup>37</sup> was reproduced for comparison with the continuous synthesis. The results confirm that  $\text{Zn}_3\text{N}_2$  QDs can be generated from  $\text{ZnEt}_2$  and  $\text{NH}_3$  as precursors. The fluorescence wavelength maximum logarithmically increases with cyclic  $\text{ZnEt}_2$  injections at 225 °C (Fig. S1†). In detail, the slope is steep from 503 to 620 nm and flattens at higher emission wavelengths. Besides that, a lower amount of added  $\text{ZnEt}_2$  precursor (0.25 mmol) results in smaller wavelength gradations with the same slope behaviour. From a kinetic point of view, the reaction solutions immediately changes colour from transparent to honey-yellow after the initial  $\text{ZnEt}_2$  injection in the right precursor ratio whereas a lasting fluorescence can be detected after ~2.5 min after the 1st or 3th–4th  $\text{ZnEt}_2$  injection at 225 or 190 °C, respectively. Within the vessel, however, the fluorescence colour continuously red shifts until the fraction is collected over the course of 5 min. The wavelength slope in this study resembles the results suggested by P. Taylor *et al.* ( $\text{NH}_3$  flow of  $5 \text{ ml min}^{-1}$ ).<sup>37</sup> Here, a  $\text{NH}_3$  flow lower than  $10 \text{ ml min}^{-1}$ , however, causes black precipitation as  $\text{ZnEt}_2$  decomposes without further conversion into Zn and ethane.<sup>47</sup> The same happens with too fast  $\text{ZnEt}_2$  injections (<20 s) which causes reflux and interruption of the ammonia gas flow. P. Taylor *et al.* already described the precursor ratio to be crucial for nucleation and



growth detailing that higher  $\text{ZnEt}_2$  starting concentrations did not result in well-defined emission peaks.<sup>37</sup>

190 °C turns out to be the minimal reaction temperature needed (Fig. S1†). Lower reaction temperatures (100, 150 °C) lead to white precipitation, presumably  $\text{ZnO}$ . Too long pre-heating (0.45 h) of oleylamine in 1-octadecene at 225 °C causes gelification. The wavelength variance per  $\text{ZnEt}_2$  injection increases with particle size (Fig. S1†). In other words, the slower nanoparticle growth succeeds differently for each batch concluded from the large standard deviations (4–47 nm) between various batches using the same synthesis conditions (Fig. S1†). The reproducibility is even less consistent for 190 °C. Each batch delivers a different nanoparticle growth rate (Fig. S1†).

In conclusion, homogenous heat and precursor distribution are decisive for the generation of  $\text{Zn}_3\text{N}_2$  nuclei/clusters to suppress both side products (presumably  $\text{ZnO}$  and  $\text{Zn}$ ). The nanoparticle growth is not uniform in batchwise synthesis. Specifically, homogeneity within the vessel determines the contact probability of both precursors. At constant magnetic stirrer rate, the gas pressure defines solubility and mixing state in the case of ammonia. The injection speed determines the mixing state in the case of  $\text{ZnEt}_2$ . Both factors mutually interact as ethane gas is released with 6 mol equivalents in the reaction course  $[3\text{Zn}(\text{C}_2\text{H}_5)_2, \text{liquid} + 2\text{NH}_3, \text{gas} \rightarrow \text{Zn}_3\text{N}_2 \downarrow + 6\text{C}_2\text{H}_6 \uparrow]$ .

## Continuous synthesis

### Technical and material requirements

A safe continuous synthesis is feasible for  $\text{Zn}_3\text{N}_2$  QDs. This accomplishment results from fulfilling technical as well as

material requirements. With respect to the experimental setup, both batch and continuous flow synthesis have the  $\text{NH}_3$  gas-handling components in common (Fig. 2 and S2†), requiring a corrosion-protected pressure regulator (Fig. 2①) followed by a three-way-stop-cock (Fig. 2②) to quickly exchange the back flushing gas ( $\text{N}_2$ ) with the reaction gas. The mass flow controller is equipped with Kalrez gaskets also due to the corrosive properties of  $\text{NH}_3$ . Sufficient ammonia flow rate can be supplied by the employed gas cylinder at room temperature as predicted using thermodynamic process simulation (Fig. S3†). In detail, regulation of pressure has the largest influence on the withdrawal amount as gas phase only compared to the influences of water impurities within the gas cylinder or room temperature variations. Experimentally, the pressure sensor detects pressure drops between 1.8 and 2.3 bar during a continuous synthesis session within the pipe system. Electrical heating pads (Fig. 2③) are used as heat sources to prevent re-condensation of ammonia inside the mass flow controller. A check-valve (Fig. 2④) with 0.03 bar opening pressure prevents reflux to the instruments.

With respect to the second precursor,  $\text{ZnEt}_2$ , two reservoir bottles are flushed with inert gas ( $\text{N}_2$ ). One bottle contains  $\text{ZnEt}_2$  stock in 1-octadecene and the other neat 1-octadecene for additional inline dilution. Two piston pumps create stable flows as recorded by two individual mass flow controllers. The  $\text{ZnEt}_2$  component is further diluted using a slit-interdigital micro mixer (Fig. 2⑤) to create flow-dependent input concentrations (Fig. S4†). Both reaction partners join with the help of a T-mixer (Fig. 2⑥) which creates a segmented flow inside a transparent FEP capillary at room temperature (Fig. S5†). At the reactor outlet, gas–liquid

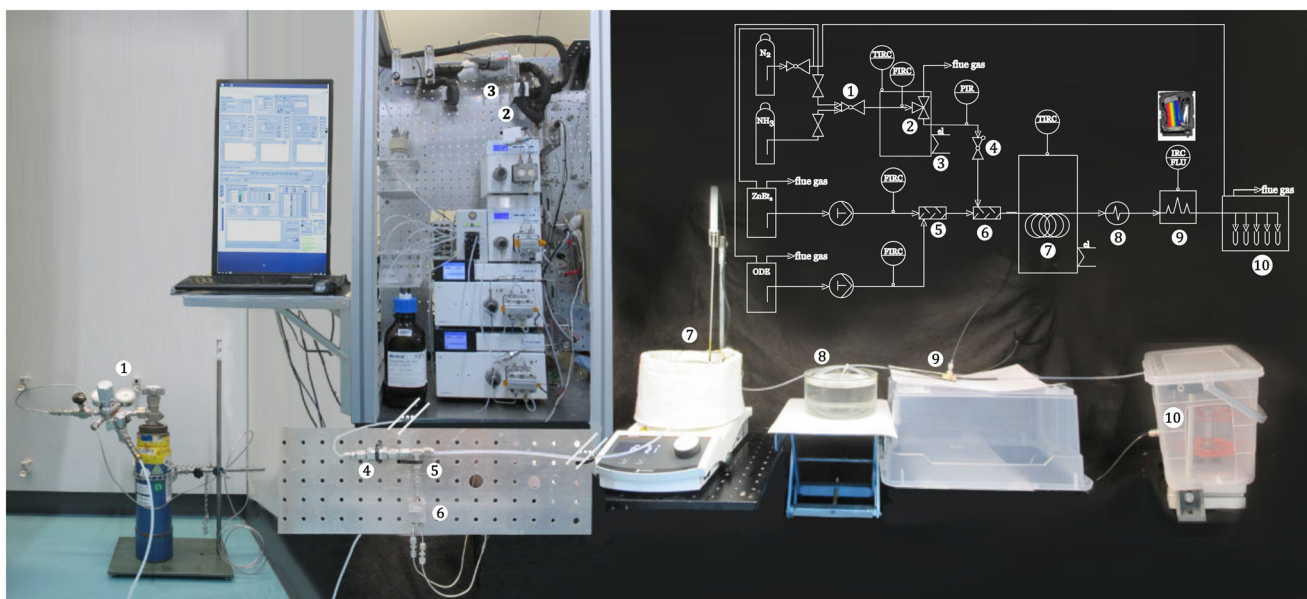


Fig. 2 Photo collage of the experimental setup of the process and P&ID diagram. For  $\text{Zn}_3\text{N}_2$  continuous synthesis, the precursors  $\text{NH}_3$  ①–④ and diethylzinc ( $\text{ZnEt}_2$ ) are used. For inline dilution ⑤, the solvent 1-octadecene (ODE) is applied. Controlling units adjust all mass flows. Both precursors are mixed with the help of a static mixer ⑥ before they enter the heat ⑦ and cooling zone ⑧. The synthesis product's emissive properties are then measured within an optical flow cell ⑨ before they are collected at inert gas conditions ⑩.



segments are not as periodic as at the beginning (Fig. S5†), which can be explained by the gas expansion and changed wetting properties at higher temperatures.

A white solid deposit is gradually formed at the tube wall just before the tube reactor enters the heating zone (Fig. 2⑦). Presumably, this is ZnO that is formed in a side reaction at lower temperature, also observed in the batch synthesis below the onset temperature for  $\text{Zn}_3\text{N}_2$  of 190 °C. A more instant temperature transition would minimise this side reaction and the amount of deposited material. As known for ZnO, the residue can be completely dissolved with diluted acetic acid to clean the reactor before priming with 1-octadecene to wet the hydrophobic tube surfaces again before synthesis.

After cooling (Fig. 2⑧) with the help of a waterbath, a fibre-optic assembly (Fig. 2⑨) around the transparent tube reactor allows measuring the fluorescence signals in the running process. In this context, 455 nm or higher excitation wavelengths avoid confusion with oleylamine's autofluorescence, the surfactant in use (Fig. S6†).

To prevent contact with the atmosphere, the fraction collector is sealed in a box (Fig. 2⑩) flushed with  $\text{N}_2$ . The  $\text{Zn}_3\text{N}_2$  nanoparticles exhibit a fast decrease of fluorescence in the presence of water and oxygen in atmosphere<sup>40</sup> as well as in insufficiently dried solvents (Fig. S7†). The degradation is visible as the wavelength maximum shifts to shorter wavelength (Fig. S7†). Precipitation and re-dispersion do not effect the spectral features when thoroughly dried solvents are used.

The determined average residence times correlate well with the theoretical times based on the reactor volume of 24 ml (Fig. S8†). To ensure static conditions after changing process parameters, 1–2 times the reactor volume was discarded before the synthesis fraction was collected.

## Product evaluation

The inherent product quality is equally good comparing batch and continuously manufactured  $\text{Zn}_3\text{N}_2$  QDs.

Continuously manufactured, a broad spectrum of emission wavelengths can be synthesised ranging from 506 to 710 nm (Fig. 3). Higher emission wavelengths are expected when increasing the input concentrations analogue to batchwise production. Inherently,  $\text{Zn}_3\text{N}_2$  offers a high colour brilliance as defined by the *International Commission on Illumination*, displayed by the CIE colour gamut (Fig. 3). Batchwise and continuously synthesised products show a similar, high colour brilliance, for orange and red emitting QDs in particular.

As expected from the quantum confinement effect, the emission wavelength increases with nanoparticle size (Fig. 4 and S9†). In detail, green and orange emitting QDs are small with 4 nm in average albeit they cannot be further differentiated. Red and dark-red QDs have a circular equivalent diameter of 7 and 10 nm in average, emitting at 644 and 684 nm, respectively. The average sizes presented here are comparable to the particle sizes reported previously<sup>43</sup> for low emission wavelength peak positions. They are larger in average for red emitting QDs. This discrepancy could be due to the total number of considered objects or due to uncertainty with the interpretation of the particle edges which are demanding considering the microscopic resolution in this small size and atomic number range. With respect to the atomic composition, energy electron loss spectroscopy qualitatively confirms a Zn–N compound (Fig. S10†). It also detects oxygen as an indication of ZnO as a side product. However, ZnO would be expected exclusively if mounting to the microscope at  $\text{N}_2$  atmosphere had leaked because of the fast decomposition rate (Fig. S7†).

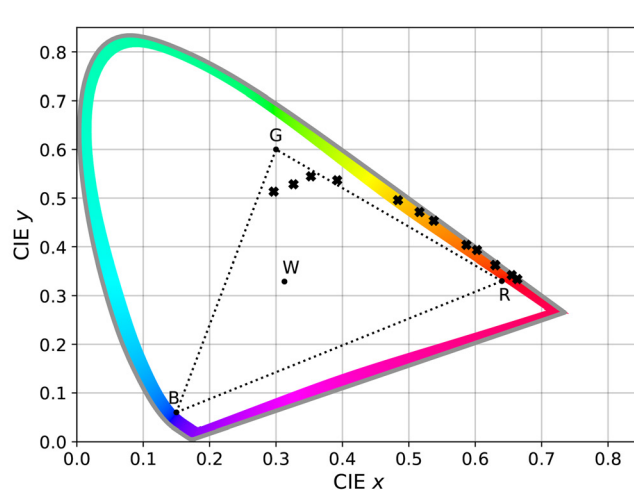
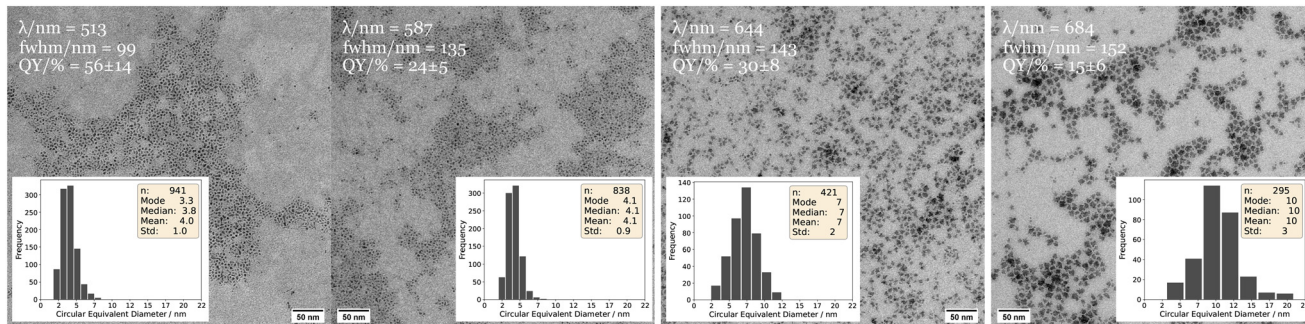


Fig. 3 Photograph of continuously synthesised  $\text{Zn}_3\text{N}_2$  samples at UV-light (left) and their corresponding coordinates in the CIE colour map (right). A broad fluorescence wavelength spectrum can be manufactured in a continuous synthesis manner, namely 506 to 710 nm (left).  $\text{Zn}_3\text{N}_2$  QDs inherently offer high colour purity as their emission spectra correspond to CIE coordinates at the edge of the respective colour gamut (right). Here, the dotted triangle spans the standardised Adobe RGB (1998) colour space, thus  $\text{Zn}_3\text{N}_2$  QDs exceed this region.





**Fig. 4** TEM images at the same magnification level of continuously synthesised Zn<sub>3</sub>N<sub>2</sub> QDs samples. Their spectral properties are summarised in each caption and their size distributions are presented as histograms including their statistical analysis. The average circular equivalent diameter and size dispersity increase from green to red emitting Zn<sub>3</sub>N<sub>2</sub> QDs (4 ± 1 ± 10 ± 3 nm). Conversely, the quantum yield was found to be the highest for green and decreases towards red emitting nanocrystals.

With respect to quality criteria, the full widths at half emission maximum (FWHM) are large for batch as well as for continuously fabricated QDs, the latter being equal or up to 9 nm larger at comparable wavelength positions. They FWHM ranges from 99 for green to 186 nm for dark-red emitting nanocrystals (Fig. S11†). This feature can be interpreted as a dispersity indicator of the ensemble since QDs of different sizes contribute to the spectrum. Conversely, this characteristic correlates with the nanoparticle size distribution which also increases towards red emitting QDs according to the microscopic results (Fig. 4). In detail, the microscopic images suggest occasional interparticle growth since some nanoparticles appear to have joined together in a double-sized rod-like shape. A second nucleation of smaller nanoparticles could also result in increased particle size dispersity although oleylamine has demonstrated fast monomer release for nanoparticle nucleation as complexation partner, mostly observed in comparison to its common teammate oleic acid.<sup>12,48,49</sup> It should be noted that technical-grade oleylamine was used in this, as in most, studies which contains mainly trans and cis oleylamine but also luminescent C<sub>18</sub>-amides or nitroalkanes impurities whose impacts on nucleation are not evaluated yet selectively.<sup>50</sup> The microscopic images of the Zn<sub>3</sub>N<sub>2</sub> QDs further disclose an increase of windrose shaped nanoparticles with increasing size (Fig. S9†) while the aspect ratio remains similar for all size categories. This indicates atomic addition to selective crystal facets in relation to the monomer amount available comparable with Pt<sub>3</sub>Fe nanoparticles.<sup>51</sup>

Another quality characteristic is the fluorescence quantum yield. The results show the highest value for green (56 ± 14%) and the smallest for red emitting QDs (15 ± 6%) (Fig. 4 and S12†). For analysis, rhodamine 6G is used as reference material because its emission properties are more stable in hygroscopic solvents like ethanol or 1,4-dioxane than other candidates, like Nile Red when using low concentrations (<10<sup>-5</sup> mol L<sup>-1</sup>).<sup>52-55</sup> In theory, a lowered quantum yield of QDs is the result of exciton trapping states of non-coordinated surface atoms of the nanoparticle. This

physicochemical effect is more likely for larger nanoparticles because the nanoparticles surface increases. Using computational bonding studies, this idea was confirmed for previous QDs systems with Z-type ligands as bonding partners.<sup>44</sup> In this study, post-synthetic experiments show a higher luminescence of the Zn<sub>3</sub>N<sub>2</sub> QDs when adding additional oleylamine or stronger Lewis bases. Latter solidify the chemical bonding between ligands and surface atoms because ligand solvation competes with surface coordination. In detail, tertiary phosphines show to be more effective to create higher luminescence than amines (Fig. S13†).

Overall, the obtained quantum yield values of Zn<sub>3</sub>N<sub>2</sub> are relatively high compared to other common core QDs considering that no additional shell material is applied yet which can increase the quantum yield and also the absorption cross section. Cu<sub>3</sub>N could be a suitable shell candidate because crystal growth seems realistic at the phase boundary. The distortion of the coordination octahedra with Cu<sub>3</sub>N would be max. 0.5 Å, 11°<sup>56,57</sup> and could be addressed in a future study. Band gap energies of 1.4 and 2.1–3.7 eV were found experimentally for Cu<sub>3</sub>N bulk materials as well as a work function of around 4.5 eV.<sup>58,59</sup> This could result in a type 1 or quasi-type 2 band alignment with Zn<sub>3</sub>N<sub>2</sub> taken the theoretical value of 4.2 eV for the work function of Zn<sub>3</sub>N<sub>2</sub> into account based on bulk material studies.<sup>60</sup>

### Process evaluation

The continuous synthesis process offers savings on time, reagent gas consumption and ultra-dry solvents.

The most decisive time saving results from the higher mass transfer compared to the batchwise synthesis because ammonia gas is captured within the reaction medium compared to the rinsing bubbles in a flask. This results in a higher surface area to volume ratio and in turn increases the contact probability with ZnEt<sub>2</sub> per volume unit. As a consequence, QDs of a specific size can be produced without the need of stepwise ZnEt<sub>2</sub> additions. As an example, QDs grow towards red emission (>620 nm) at 225 °C after 4 individual ZnEt<sub>2</sub> injections which equals 20 min during batch



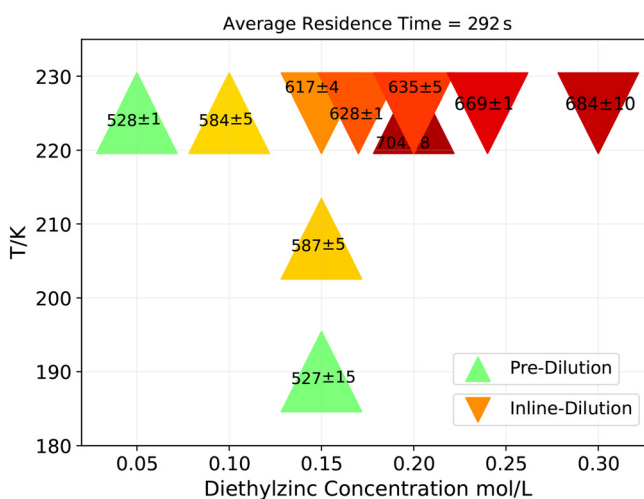
synthesis (Fig. S1†). In contrast, the same colour range can be obtained in a single process-step with the same  $\text{ZnEt}_2$  concentration after 7–10 min in flow synthesis including the time until the same product volume is obtained as in batch synthesis (31 ml). This is an enhancement of *circa* 50 percent for red emitting quantum dots. Reagent gas is also saved as a consequence of the overall shorter manufacturing time while the  $\text{ZnEt}_2$  input concentrations are variable and in the same magnitude as for batchwise synthesis. In more detail, a mass flow rate of 3–10  $\text{ml min}^{-1}$  is used for  $\text{NH}_3$ . This equals a molar excess of ~2–3 in relation to the  $\text{ZnEt}_2$  mass flow, taking into account  $\text{NH}_3$ 's volume expansion at reaction temperature at the given system pressure within the tube reactor which was recorded inline. Smaller molar excesses than 2–3 are conceivable in future works which would allow the use of even less gas supply and a wider residence time range than 2.5–30 min within the same experimental setup.

With respect to the reproducibility, the continuous setup is slightly superior in comparison to batch results concluded from the standard deviations of the emission peak over several flow runs with the same process conditions (Fig. 5 and S1†) comparing the results at similar wavelength positions. They are smaller and the reproducibility is higher in the case of the continuous process. With respect to the impact of the process parameter Average Residence Time, the results are not fully conclusive yet because of the magnitude of standard deviations. This is most probably caused by the aforementioned pressure variations in the system. In future works, it can be further investigated whether the same results can be obtained with even less Average Residence Time to exploit the technical opportunities. The reaction temperature shows the largest impact to tune the wavelength maxima, next to the  $\text{ZnEt}_2$  concentration. Latter results in a logarithmic increase

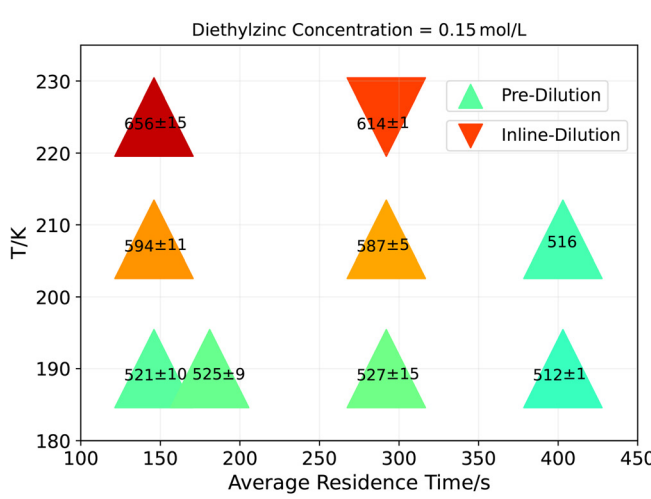
(Fig. 5). In detail, large wavelength shifts of 27–73 nm and 7–34 nm can be obtained varying temperature and concentration, respectively, while changing the residence time show the lowest impact to tune the wavelength maxima with 2–15 nm for the wavelength shift. As a consequence, the same wavelength can be obtained at 208 °C with 0.15 M  $\text{ZnEt}_2$  or at 225 °C with only 0.1 M  $\text{ZnEt}_2$ . The reaction mixture or preheated  $\text{ZnEt}_2$  precursor convert to more Zn or  $\text{ZnO}$  side products with increasing starting concentration. In future works, more insulation should be provided before heat contact.

Next to improved mass and heat transfer within the microfluidic reactor, process automation also results in time optimisation. At first, preparation effort is reduced thanks to the inline dilution of  $\text{ZnEt}_2$ 's starting concentration. In detail,  $\text{ZnEt}_2$  stock solution was initially pre-diluted with the solvent 1-octadecene and then inline-diluted during the flow synthesis using the slit interdigital micromixer (Fig. S4†). In comparison, pre-dilutions requires more preparation time at inert gas conditions which results in less flexibility during synthesis. Inline-dilution causes shorter emission wavelengths in a reproducible manner based on the standard deviation of the emission peaks (Fig. 5). This could be due to higher pressure drop registered when using the slit interdigital micromixer compared to the process with pre-dilution. As a consequence, the ammonia gas segments and contact area to  $\text{ZnEt}_2$  are smaller.

Apart from inline concentration adjustment, the inline analytical setup reliably notifies precursor conversion to the product after the target average residence time. Furthermore, the optical flow measurement delivers emission data which highly agree with the offline emission results (Fig. 6 and S14†). In this context, a baseline drift was observed which is negligible for the peak analysis. Overall, the analytical device



**Fig. 5** Fluorescence emission maxima of continuously manufactured  $\text{Zn}_3\text{N}_2$  QDs as a function of  $\text{ZnEt}_2$  concentration (left), residence time (right) and reaction temperature (left and right). Standard deviations result from replicate syntheses. Reaction temperature shows the largest impact on the fluorescence emission wavelength position compared to  $\text{ZnEt}_2$  concentration and residence time.  $\text{ZnEt}_2$  stock solution was either pre-diluted with the solvent 1-octadecene ( $\Delta$ ) or inline-diluted ( $\nabla$ ) during the flow synthesis using the slit-interdigital static mixer (Fig. S4†). In comparison, latter causes smaller wavelength peak positions.



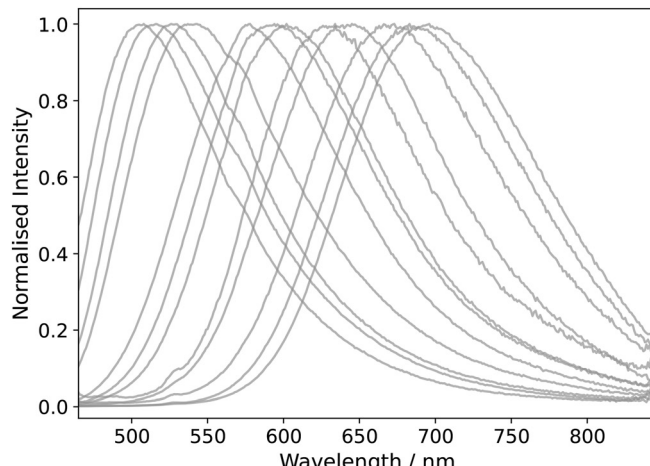


**Fig. 6** Offline fluorescence emission spectra of selected  $\text{Zn}_3\text{N}_2$  samples on the left (same samples as in Fig. 3) which highly correlate with inline measured emission peak positions as shown on the right. Consequently, integration of optical flow cells can reduce preparation time and exposure of the water/oxygen sensitive material alongside the continuous synthesis.

results in time-saving because the process parameters can be regulated in real-time. Moreover, the analytical setup reduces measurement effort in order to obtain the product's spectroscopic properties. This includes drying of organic solvents and measurement preparation under inert gas condition. For a more in-depth analysis, the exposure of  $\text{Zn}_3\text{N}_2$  to the atmosphere can be minimised to pre-selected samples based on the inline obtained analysis results.

## Conclusions and outlook

This work outlines the realisation of the continuous flow synthesis of  $\text{Zn}_3\text{N}_2$  quantum dots, providing a safe solution despite its hazardous starting components  $\text{NH}_3$  and diethylzinc, for the first time. The described procedures provide handling recommendations for future works with  $\text{Zn}_3\text{N}_2$  nanoparticles. Overall, the technical investment is beneficial because of time, gas and solvent savings in comparison to the batch-to-batch approach. Moreover, the continuous process offers the advantages of fine-tuning the optical properties and straight-forward synthesis at preparative scale.

Future work is directed towards an adequate shell material in a multistage process in order to increase the chemical stability of the core quantum dots. From a technical point of view, additional analytical devices like gas sensors could determine the turnover rate during  $\text{Zn}_3\text{N}_2$  production which would allow further optimisation of mass flows, reagent and time savings.

## Experimental section

### Batch synthesis

For batch synthesis, disclosed procedure steps were adopted from the previously mentioned protocol.<sup>37</sup> In detail, 1-oleylamine (OLA, 70%), 1-octadecene (ODE, 90%) and 1.0

M diethylzinc ( $\text{ZnEt}_2$ ) in hexanes were purchased from J&KScientific (San Jose, CA, USA) and (Merck KgaA, Germany), respectively. The organic synthesis components were stored at inert gas condition ( $\text{N}_2$ ) and used without further purification. A corrosion-resistant pressure regulator was employed for the  $\text{NH}_3$  gas bottle (99.98%, Linde, Dublin, Ireland) (from 8.5 to 5 bar) while  $\text{N}_2$  was used as flushing gas. Electrical heating pads guaranteed a temperature level of *ca.* 50 °C for the gas flow meter (Thermal GAS Mass Flow Meter Controller, EL-FLOW Select F-201CV/Bronkhorst, Gelderland, The Netherlands). The gas component was introduced into the rubber sealed round bottom flask (50 ml) at a rate of 10 ml min<sup>-1</sup> using a steel injection needle (0.8 × 120 mm) which was pierced through the septum as well as a thermocouple for temperature control. 30 ml 1-octadecene and 1 ml oleylamine were heated to reaction temperature (190 or 225 °C) at constant stirring rate of 500 U min<sup>-1</sup> for 10 min prior to  $\text{ZnEt}_2$  injection. 1.0 mmol of  $\text{ZnEt}_2$  was periodically injected into the solution at 5 min intervals which equalled 1 ml of the  $\text{ZnEt}_2$ -hexane stock solution. The fraction collection from the vessel was performed passively *via* a second needle supported by the positive pressure within the vessel. The whole procedure was performed within a glovebox (MBraun, Garching, Germany) under inert conditions using  $\text{N}_2$ .

### Continuous synthesis

The same chemicals were used as for the batch synthesis. In contrast,  $\text{ZnEt}_2$  was introduced in a single process step and was either diluted with ODE beforehand or during flow synthesis (0.05–0.3 mol l<sup>-1</sup>). The  $\text{ZnEt}_2$  reservoir was prepared inside the glovebox and stirred for 5 min at 500 U min<sup>-1</sup>. Sensors informed about the water and oxygen content within the glovebox which did not exceed above 3 ppm. In addition, magnetic stirring bars were heated out at 110 °C over night



before use. In this context, the same OLA concentration was applied (3 vol%) as for batch synthesis within the reservoir. Both liquid components ( $\text{ZnEt}_2$ , ODE) reservoirs were flushed with  $\text{N}_2$  during continuous synthesis while the whole setup was stored in a fume hood at atmospheric conditions. Initially, solely  $\text{N}_2$  gas and ODE wetted the tube reactor (PTFE, 1/8", 12 m, ID = 1.6 mm) until the reaction temperature was reached (190, 208, 225 °C) using an oil bath and a hotplate with internal temperature regulation (Pt1000-thermocouple, Heidolph MR Hei-Tec, Schwabach, Germany). For online analysis, fluorescence signals were recorded using a CCD spectrometer (ULS2048L-RSUSB2 from Avantes, Apeldoorn, Netherlands). For this purpose, a self-built flow cell was applied based on a 5-port union (P-155, IDEX H&S, WA 98277, USA). The tube reactor itself served as the light path (3.2 mm) while fibre optics were aligned (M113L02 Thorlabs, NJ, USA) in a 90° geometry after excitation at 455 nm using a light-emitting diode. Optical emission spectra between 300 and 900 nm were recorded periodically with 1 Hz acquisition rate.  $\text{ZnEt}_2$  and ODE were delivered simultaneously utilising 10 ml piston pumps (Knauer 40P, Berlin, Germany). The flow rate of each component was electronically captured using mass flow meters (mini Cori-Flow/Bronkhorst, Gelderland, Netherlands), which allowed the adjustment of all concentrations in the resulting flow going into the reactor. In addition, the system pressure drop was determined with a pressure sensor (Little Things Factory, Elsoff, Germany), followed by a check-valve (No.: SS-2C-1/3, Swagelok, Solon, OH, USA). For inline dilution of  $\text{ZnEt}_2$ , homogenous mixing was accomplished using the slit-interdigital micro mixer, developed and manufactured at Fraunhofer IMM (Mainz, Germany).<sup>61–63</sup> The segmented gas-liquid flow was realised using a T-mixer (No.: SS-200-3, Swagelok, Solon, OH, USA). Four average residence times were considered (146, 181, 292, 403 s), adjusting all three streams relatively to the total stream flow. To cool the reaction medium, heat exchange was realised at the interface between water and the tube reactor (0.08 m). Serial to the capillary heat exchange, fluorescence properties were thus recorded at room temperature. At the end, a self-built fraction collector comprising a vial holder on top of a stepper motor switched between product and rinsing step, while being flushed with  $\text{N}_2$  to provide inert conditions. By default, 1–2 times the reactor volume was used for rinsing before product collection. To fully control the flow pilot plant, a LabVIEW program (version 2018) was developed for managing the individual components and to visualize and record the process and optical spectra data.

### Residence time distribution

The mean residence time distribution was estimated *via* pulse experiments at 190 °C starting from the 2-phase flow ( $\text{NH}_3$  and ODE). In detail, Nile Red dye was used as tracer material which was dissolved in ODE and ethanol (4 vol% (ref. 17)), the latter to provide brighter intensity.

### $\text{NH}_3$ mass flow simulation

In order to simulate the withdrawal of anhydrous gaseous ammonia from a steel cylinder, an equivalent process model is developed based on the publication by AirLiquide<sup>64</sup> using the ProSim Plus software (version 3.7.4.0, physicochemical properties taken from ProSim Simulis version 2.0.42, Peng–Robinson thermodynamic model). The simulation flowsheet of the process model is illustrated in the ESI† to this publication (Fig. S3†). The steel cylinder (ammonia purity: 99.98%; cylinder volume: 2 L; vendor: Linde Gas AG, Höllriegelskreuth) is represented by a generalised heat exchanger model with an exchange area of  $A: 0.064 \text{ m}^2$  and a clean overall heat transfer coefficient of  $5.56 \text{ W m}^{-2} \text{ K}^{-1}$  (labelled CYCLINDER in Fig. S3†) and heated by an air flow with a flow rate of  $1700 \text{ Nm}^3 \text{ h}^{-1}$  and air temperatures of 20 to 24 °C (stream ATM-1 in Fig. S3†), which were observed under the fume hood used for the experiments. The ammonia feed flow (flow NH3-LIQ in Fig. S3†) is chosen in such a way that a vapor fraction of  $\geq 0.9991$  is observed at the outlet of the steel cylinder model (flow NH3-VAP-HP in Fig. S3†) in order to determine the maximum gaseous ammonia threshold quantity for a specified pressure, air flow, air temperature and contamination of the ammonia with water. Ultimately, the ammonia flow is specified as a volume flow in the unit of  $\text{mL min}^{-1}$  based on standard conditions (STP: 273.15 K; 101.325 Pa).

### Purification & ligand testing

Toluene anhydrous and acetonitrile anhydrous (99.8%, Merck KgaA, Germany) were additionally dried, first over 5 vol% regenerated molecular sieve (4 Å) for 1 week. In addition, toluene and acetonitrile were then distilled for *ca.* 2 h over metallic sodium and  $\text{CaH}_2$ , respectively. Both were stored at inert gas conditions hereafter.

For microscopic analysis,  $\text{Zn}_3\text{N}_2$  QDs were separated from the oily synthesis components (ODE, OLA) *via* precipitation and dispersion, twice in the case of orange and red QDs and three times in the case of green QDs. In detail, sample raw material was diluted in ultra-dry toluene by a factor of 4 ( $df = 4$ ). The solutions blurred adding profoundly dried acetonitrile (40 vol%) which was more evident for larger, red than smaller, green QDs. Relative centrifugal force (2000g, Sigma 1–16k) supported the nanoparticle's sedimentation for 10 min before they were redispersed in fresh toluene to obtain the original dilution factor. The whole purification procedure was performed in a glovebox flushed with  $\text{N}_2$ .

Different surfactants were evaluated after replacing the raw solvent volume with a different surfactant volume. In detail, red QDs were sedimented for 20 min with relative centrifugal force of 20 627g and redispersed in ODE and new surfactant (5 mol equivalent in relation to the  $\text{ZnEt}_2$  concentration: tributylphosphine, trioctylphosphine, 1-octanethiol, 1-dodecanethiol, 1-octanol, 1-undecanol, butylamine). After a 12 h storage at room temperature, the materials were compared with a hand-held UV lamp.



# Characterisation

## Spectroscopy

Off-line optical spectroscopy was performed with a Cary 50-Scan and a Cary Eclipse for UV/vis and fluorescence spectroscopy, respectively (Agilent Technologies, Santa Clara, CA, USA). This setup provides analysis in a spectral range between 300 and 900 nm. Raw materials were measured within additionally-dried toluene and airtight quartz cuvettes ( $d = 1$  cm, Hellma, Müllheim, Germany) which were dried over night at 110 °C and sealed at inert gas condition for both, blank and sample analysis. As excitation wavelengths, 455 and 480 nm were used. A time gap of 5 min was applied between replicates to evaluate the stability of the emission wavelength position. Offline signals were corrected by wavelength dependent calibration factors according to the manufacturer. CIE coordinates were calculated with the help of a python script.<sup>65</sup> Photoluminescence quantum yields were determined relatively to an organic fluorophor.<sup>66</sup> As external standard, Rhodamine 6G in isopropanol was used (99.99%, Merck KgaA, Germany) assuming a quantum yield of 95%.<sup>67</sup> Confidence intervals (upper and lower) were determined of both linear regression slopes (reference and sample).<sup>68</sup> In this context,  $\alpha = 0.05$  was used for the Student's *t*-distribution. The quantum yield is based on the relation between sample and reference and so is the total error based on the upper sample confidence interval and the lower reference confidence interval.

## Transmission electron microscopy (TEM) & electron energy loss spectroscopy (EELS)

For visualisation of the  $Zn_3N_2$  QDs, the purified synthesis solutions were diluted in additionally-dried toluene ( $df = 100$ ). Then, they were dried on carbon-coated copper grids. The manual transfer to the microscope sample holder succeeded at inert gas condition with the help of liquid and gaseous nitrogen. TEM measurements were performed with a Zeiss Libra 120 electron microscope (Zeiss, Oberkochen, Germany) at 120 kV acceleration voltage for imaging and for spectroscopy. The images were taken by a CCD camera. The circular equivalent diameter  $[(4 \times \text{area}/\pi)^{1/2}]$  and the size distribution of the nanoparticles were determined by manually retracing the shape within 2 to 4 images. Prior, the grey scaled raw images were processed using a median filter (5 px radius) and contrast factor (0.3%) provided by the software package ImageJ.

## Data availability

Data supporting this article have been included as part of the ESI.<sup>†</sup>

## Author contributions

Malin G. Lüdicke: writing – original draft, writing – review & editing, conceptualization, investigation, methodology, validation, data curation, formal analysis, visualization. Jonas

Schramm: writing – review & editing, conceptualization. Martin Wichert: software, formal analysis and Ralph A. Sperling: writing – review & editing, conceptualization, investigation, resources.

## Conflicts of interest

There are no conflicts to declare.

## Notes and references

- 1 J. Mondal, R. Lamba, Y. Yukta, R. Yadav, R. Kumar, B. Pani and B. Singh, *J. Mater. Chem. C*, 2024, **12**, 10330–10389.
- 2 A. A. H. Abdellatif, M. A. Younis, M. Alsharidah, O. Al Rugaie and H. M. Tawfeek, *Int. J. Nanomed.*, 2022, **17**, 1951–1970.
- 3 A. Fleming MD, Diabetes Autoimmunity Withdrawn In New Onset and In Established Patients (SUNRISE): NIH Identifier: NCT03895437.
- 4 J.-H. Han and H.-K. Park, Samsung Electronics Co., Ltd. – 2024 1Q Interim Business Report, [https://images.samsung.com/is/content/samsung/assets/global/ir/docs/2024\\_1Q\\_Interim\\_Report.pdf](https://images.samsung.com/is/content/samsung/assets/global/ir/docs/2024_1Q_Interim_Report.pdf).
- 5 M. Hao, Y. Bai, S. Zeiske, L. Ren, J. Liu, Y. Yuan, N. Zarrabi, N. Cheng, M. Ghasemi, P. Chen, M. Lyu, D. He, J.-H. Yun, Y. Du, Y. Wang, S. Ding, A. Armin, P. Meredith, G. Liu, H.-M. Cheng and L. Wang, *Nat. Energy*, 2020, **5**, 79–88.
- 6 K. Watanabe, Y. Orimoto, K. Nagano, K. Yamashita, M. Uehara, H. Nakamura, T. Furuya and H. Maeda, *Chem. Eng. Sci.*, 2012, **75**, 292–297.
- 7 S. Marre, J. Park, J. Rempel, J. Guan, M. G. Bawendi and K. F. Jensen, *Adv. Mater.*, 2008, **20**, 4830–4834.
- 8 J. Baek, Y. Shen, I. Lignos, M. G. Bawendi and K. F. Jensen, *Am. Ethnol.*, 2018, **57**, 10915–10918.
- 9 C. Ippen, B. Schneider, C. Pries, S. Kröpke, T. Greco and A. Holländer, *Nanotechnology*, 2015, **26**, 085604.
- 10 A. M. Nightingale, J. H. Bannock, S. H. Krishnadasan, F. T. F. O'Mahony, S. A. Haque, J. Sloan, C. Drury, R. McIntyre and J. C. deMello, *J. Mater. Chem. A*, 2013, **1**, 4067.
- 11 A. Schiener, A. Magerl, A. Krach, S. Seifert, H.-G. Steinrück, J. Zagorac, D. Zahn and R. Wehrich, *Nanoscale*, 2015, **7**, 11328–11333.
- 12 M. Abolhasani, C. W. Coley, L. Xie, O. Chen, M. G. Bawendi and K. F. Jensen, *Chem. Mater.*, 2015, **27**, 6131–6138.
- 13 M. Herbst, E. Hofmann and S. Förster, *Langmuir*, 2019, **35**, 11702–11709.
- 14 S. Krishnadasan, R. J. C. Brown, A. J. deMello and J. C. deMello, *Lab Chip*, 2007, **7**, 1434–1441.
- 15 Y. Orimoto, K. Watanabe, K. Yamashita, M. Uehara, H. Nakamura, T. Furuya and H. Maeda, *J. Phys. Chem. C*, 2012, **116**, 17885–17896.
- 16 K. Abdel-Latif, R. W. Epps, F. Bateni, S. Han, K. G. Reyes and M. Abolhasani, *Adv. Intell. Syst.*, 2021, **3**, 2000245.
- 17 M. G. Lüdicke, J. Hildebrandt, C. Schindler, R. A. Sperling and M. Maskos, *Nanomaterials*, 2022, **12**, 1983.



18 A. Schejn, M. Frégniaux, J.-M. Commengé, L. Balan, L. Falk and R. Schneider, *Nanotechnology*, 2014, **25**, 145606.

19 W. Yang, H. Yang, W. Ding, B. Zhang, L. Zhang, L. Wang, M. Yu and Q. Zhang, *Ultrason. Sonochem.*, 2016, **33**, 106–117.

20 B.-H. Kwon, K. G. Lee, T. J. Park, H. Kim, T. J. Lee, S. J. Lee and D. Y. Jeon, *Small*, 2012, **8**, 3257–3262.

21 R. Gresback, T. Nozaki and K. Okazaki, *Nanotechnology*, 2011, **22**, 305605.

22 T. A. Pringle, K. I. Hunter, A. Brumberg, K. J. Anderson, J. A. Fagan, S. A. Thomas, R. J. Petersen, M. Sefannaser, Y. Han, S. L. Brown, D. S. Kilin, R. D. Schaller, U. R. Kortshagen, P. R. Boudjouk and E. K. Hobbie, *ACS Nano*, 2020, **14**, 3858–3867.

23 J. Baek, P. M. Allen, M. G. Bawendi and K. F. Jensen, *Angew. Chem., Int. Ed.*, 2011, **50**, 627–630.

24 P. Cavanaugh, X. Wang, M. J. Bautista, I. J.-L. Plante and D. F. Kelley, *J. Chem. Phys.*, 2023, **159**, 134704.

25 C. Rivaux, T. Akdas, R. Yadav, O. El-Dahshan, D. Moodelly, W. L. Ling, D. Aldakov and P. Reiss, *J. Phys. Chem. C*, 2022, **126**, 20524–20534.

26 H. Ma, L. Pan, J. Wang, L. Zhang and Z. Zhang, *Chin. Chem. Lett.*, 2019, **30**, 79–82.

27 T. Akdas, M. Haderlein, J. Walter, B. A. Zubiri, E. Spiecker and W. Peukert, *RSC Adv.*, 2017, **7**, 10057–10063.

28 A. Yashina, I. Lignos, S. Stavrakis, J. Choo and A. J. deMello, *J. Mater. Chem. C*, 2016, **4**, 6401–6408.

29 J. Pan, A. O. El-Ballouli, L. Rollny, O. Voznyy, V. M. Burlakov, A. Goriely, E. H. Sargent and O. M. Bakr, *ACS Nano*, 2013, **7**, 10158–10166.

30 I. Lignos, L. Protesescu, S. Stavrakis, L. Piveteau, M. J. Speirs, M. A. Loi, M. V. Kovalenko and A. J. deMello, *Chem. Mater.*, 2014, **26**, 2975–2982.

31 I. Shestopalov, J. D. Tice and R. F. Ismagilov, *Lab Chip*, 2004, **4**, 316–321.

32 H. Yang, W. Luan, Z. Wan, S.-T. Tu, W.-K. Yuan and Z. M. Wang, *Cryst. Growth Des.*, 2009, **9**, 4807–4813.

33 S. Yao, Y. Shu, Y.-J. Yang, X. Yu, D.-W. Pang and Z.-L. Zhang, *Chem. Commun.*, 2013, **49**, 7114–7116.

34 I. Lignos, S. Stavrakis, G. Nedelcu, L. Protesescu, A. J. deMello and M. V. Kovalenko, *Nano Lett.*, 2016, **16**, 1869–1877.

35 R. M. Macejczyk, K. Dümbgen, I. Lignos, L. Protesescu, M. V. Kovalenko and A. J. deMello, *Chem. Mater.*, 2017, **29**, 8433–8439.

36 X. Liang, R. W. Baker, K. Wu, W. Deng, D. Ferdani, P. S. Kubiak, F. Marken, L. Torrente-Murciano and P. J. Cameron, *React. Chem. Eng.*, 2018, **3**, 640–644.

37 P. N. Taylor, M. A. Schreuder, T. M. Smeeton, A. J. D. Grundy, J. A. R. Dimmock, S. E. Hooper, J. Heffernan and M. Kauer, *J. Mater. Chem. C*, 2014, **2**, 4379–4382.

38 M. Zervos, C. Karipi and A. Othonos, *Nanoscale Res. Lett.*, 2013, **8**, 221.

39 R. Ayouchi, C. Casteleiro, L. Santos and R. Schwarz, *Phys. Status Solidi C*, 2010, **7**, 2294–2297.

40 A. Trapalis, J. Heffernan, I. Farrer, J. Sharman and A. Kean, *J. Appl. Phys.*, 2016, **120**, 205102.

41 C. G. Núñez, J. L. Pau, M. J. Hernández, M. Cervera, E. Ruiz and J. Piqueras, *Thin Solid Films*, 2012, **522**, 208–211.

42 S. Carter-Searjeant, S. M. Fairclough, S. J. Haigh, Y. Zou, R. J. Curry, P. N. Taylor, C. Huang, R. Fleck, P. Machado, A. I. Kirkland and M. A. Green, *ACS Appl. Opt. Mater.*, 2023, **1**, 1169–1173.

43 R. Ahumada-Lazo, S. M. Fairclough, S. J. O. Hardman, P. N. Taylor, M. Green, S. J. Haigh, R. Saran, R. J. Curry and D. J. Binks, *ACS Appl. Nano Mater.*, 2019, **2**, 7214–7219.

44 C. Giansante and I. Infante, *J. Phys. Chem. Lett.*, 2017, **8**, 5209–5215.

45 D. Quarta, M. Imran, A.-L. Capodilupo, U. Petralanda, B. van Beek, F. de Angelis, L. Manna, I. Infante, L. de Trizio and C. Giansante, *J. Phys. Chem. Lett.*, 2019, **10**, 3715–3726.

46 A. Trapalis, I. Farrer, K. Kennedy, A. Kean, J. Sharman and J. Heffernan, *Appl. Phys. Lett.*, 2017, **111**, 122105.

47 A. A. Koski, S. J. W. Price and B. C. Trudell, *Can. J. Chem.*, 1976, **54**, 482–487.

48 G. Almeida, L. Goldoni, Q. Akkerman, Z. Dang, A. H. Khan, S. Marras, I. Moreels and L. Manna, *ACS Nano*, 2018, **12**, 1704–1711.

49 N. Bao, X. Qiu, Y.-H. A. Wang, Z. Zhou, X. Lu, C. A. Grimes and A. Gupta, *Chem. Commun.*, 2011, **47**, 9441–9443.

50 D. Baranov, M. J. Lynch, A. C. Curtis, A. R. Carollo, C. R. Douglass, A. M. Mateo-Tejada and D. M. Jonas, *Chem. Mater.*, 2019, **31**, 1223–1230.

51 C. Wang, C. Lin, B. Zhao, L. Zhang, A. Kumbhar, G. Fan, K. Sun, J. Zhang, S. Chen and J. Fang, *ChemNanoMat*, 2015, **1**, 331–337.

52 D. L. Sackett and J. Wolff, *Anal. Biochem.*, 1987, **167**, 228–234.

53 N. Ghoneim, *Spectrochim. Acta, Part A*, 2000, **56**, 1003–1010.

54 C. Würth, M. G. González, R. Niessner, U. Panne, C. Haisch and U. R. Genger, *Talanta*, 2012, **90**, 30–37.

55 U. Rocha, L. E. G. Armas, W. F. Silva, M. R. Dousti, A. L. Moura, A. Novatski, N. G. C. Astrath and C. Jacinto, *Spectrochim. Acta, Part A*, 2024, **317**, 124409.

56 U. Zachwieja and H. Jacobs, *J. Less-Common Met.*, 1990, **161**, 175–184.

57 G. Paniconi, Z. Stoeva, R. I. Smith, P. C. Dippo, B. L. Gallagher and D. H. Gregory, *J. Solid State Chem.*, 2008, **181**, 158–165.

58 A. K. Mukhopadhyay, M. A. Momin, A. Roy, S. C. Das and A. Majumdar, *ACS Omega*, 2020, **5**, 31918–31924.

59 M. I. Rodríguez-Tapiador, J. M. Mánuel, E. Blanco, E. Márquez, N. Gordillo, R. Sainz, J. Merino and S. Fernández, *Mater. Sci. Semicond. Process.*, 2025, **188**, 109176.

60 S.-H. Yoo, A. Walsh, D. O. Scanlon and A. Soon, *RSC Adv.*, 2014, **4**, 3306–3311.

61 P. Löb, K. S. Drese, V. Hessel, S. Hardt, C. Hofmann, H. Löwe, R. Schenk, F. Schönfeld and B. Werner, *Chem. Eng. Technol.*, 2004, **27**, 340–345.

62 V. Hessel, S. Hardt, H. Löwe and F. Schönfeld, *AIChE J.*, 2003, **49**, 566–577.



63 P. Löb, in *Flow chemistry*, ed. S. V. Luis and E. García-Verdugo, Royal Society of Chemistry, Cambridge, 2020, pp. 388–415.

64 B. Franz, H. Hiller, Dr. H. Müller, H. Öhmen and S. Peters, *1x1 der Gase: Physikalische Daten für Wissenschaft und Praxis*, Air Liquide Deutschland GmbH, 3rd edn, 2008.

65 M. Kness, ColorPy v1.1, <https://github.com/marknness/ColorPy>.

66 C. Würth, M. Grabolle, J. Pauli, M. Spieles and U. Resch-Genger, *Nat. Protoc.*, 2013, **8**, 1535–1550.

67 D. Magde, R. Wong and P. G. Seybold, *Photochem. Photobiol.*, 2002, **75**, 327–334.

68 L. Sachs, *Applied Statistics: A Handbook of Techniques*, Springer New York, New York, NY, 2nd edn, 1984.

